

Quantum Phase Gradient Imaging Using a Nonlocal Metasurface System

JINLIANG REN¹, JINYONG MA^{1,2}, KATSUYA TANAKA⁶,
 LUKAS WESEMANN⁴, ANN ROBERTS⁴, FRANK SETZPFANDT^{3,5},
 ANDREY A. SUKHORUKOV^{1,*}

¹*ARC Centre of Excellence for Transformative Meta-Optical Systems (TMOS), Department of Electronic Materials Engineering, Research School of Physics, The Australian National University, Canberra, ACT 2601, Australia*

²*Institute of Quantum Precision Measurement, State Key Laboratory of Radio Frequency Heterogeneous Integration, College of Physics and Optoelectronic Engineering, Shenzhen University, Shenzhen 518060, P. R. China*

³*Institute of Applied Physics, Abbe Center of Photonics, Friedrich Schiller University Jena, Jena 07745, Germany*

⁴*TMOS, Department of Electrical and Electronic Engineering, School of Physics, University of Melbourne, Melbourne, Victoria 3010, Australia*

⁵*Fraunhofer Institute for Applied Optics and Precision Engineering IOF, Albert-Einstein-Straße 7, 07745 Jena, Germany*

⁶*Institute of Solid State Physics, Abbe Center of Photonics, Friedrich-Schiller-University Jena, Helmholtzweg 5, 07743 Jena, Germany*

*Corresponding Author: Andrey.Sukhorukov@anu.edu.au

Abstract:

Quantum phase imaging enables the analysis of transparent samples with thickness and refractive index variations in scenarios requiring precise measurements under low-light conditions. Here, we present a compact quantum phase-gradient imaging system integrating a lithium niobate (LiNbO_3) metasurface for generating spatially entangled photon pairs and a silicon (Si) metasurface for phase gradient extraction. By leveraging nonlocal resonances, the LiNbO_3 metasurface enables efficient spontaneous parametric down-conversion (SPDC) with all-optically angularly tunable emission, while the Si metasurface provides a nearly linear optical transfer function (OTF) to differentiate the photon wavefunction and extract phase gradients. Experimental proof-of-concept results demonstrate the imaging of up to 25 rad/mm phase gradients with 88% fidelity over a 6×3-pixel phase object. Theoretically, the pixel resolution of the system can be enhanced by orders of magnitude by increasing the metasurface dimensions and resonance quality factor. Our work showcases the application of metasurfaces in both generating and detecting quantum states and establishes a new paradigm for portable quantum phase-gradient imaging, with potential applications in quantum sensing, microscopy, and LiDAR technology.

1. Introduction

Quantum imaging utilizing entangled photon pairs presents significant theoretical and practical advantages over classical imaging systems [1–8]. By exploiting quantum entanglement, image reconstruction can be performed through photon coincidence measurements, providing enhanced signal-to-noise ratio (SNR) [9–11], operation at ultra-low photon fluxes [5], and improved security against eavesdropping [12]. These advantages arise from the intrinsic correlations of entangled photons, which allow the extraction of information with greater efficiency than classical approaches.

Building on this foundation, quantum phase imaging [13–16] combines the strengths of quantum imaging with phase-sensitive detection [17–20], enabling the analysis of transparent samples through thickness and refractive index variations. This capability is particularly valuable in scenarios requiring non-destructive and highly precise measurements under low-light conditions.

Conventionally, the measurement of spatial phase profiles and phase gradients relied on bulky optical setups. Whereas recent advances in optical metasurfaces and thin-film structures have provided a compact alternative by realizing first-order differentiation of the optical wavefield and other mathematical operations, enabling phase-gradient extraction and edge enhancement under classical light illumination [21–26], the latter approaches remained unexplored in the realm of quantum phase imaging.

In parallel, nonlinear flat optics has emerged as a versatile platform for generating entangled photons through spontaneous parametric down-conversion (SPDC), see the reviews [27–29] and references therein. Resonance-enhanced nonlinear metasurfaces can significantly boost photon-pair generation [30] and enable precise engineering of quantum states across frequency [31, 32], momentum [33], and polarization [34–37] degrees of freedom. Such metasurfaces also offer greater environmental stability compared to conventional bulk crystals, making them attractive for free-space quantum applications. Recently, quantum ghost imaging of amplitude objects was achieved with a metasurface quantum source [38], however that scheme was insensitive to the phase variations in transparent objects.

In this work, we suggest and demonstrate experimentally novel ultra-compact approach to phase-gradient imaging through an integrated platform that uses metasurfaces for both the tasks of quantum light generation and phase-gradient extraction. Spatially entangled photon pairs are generated by a nonlinear lithium niobate (LiNbO_3) metasurface exhibiting nonlocal resonances, where the emission angle is narrow in one direction but broad in the orthogonal direction [39]. For phase-gradient extraction, a silicon (Si) metasurface with angle-sensitive nonlocal resonances is designed that allows first-order differentiation of the single-photon wavefunction and direct retrieval of the phase gradient through two-photon correlation measurements. The result is a compact and all-optically tunable system that opens promising opportunities for high-sensitivity, low-light applications in areas such as biomedical imaging, remote sensing, and secure communications.

2. Results

2.1. Concept of phase gradient imaging with single photons

We develop a scheme for phase-gradient imaging by harnessing a general framework of quantum ghost imaging, which offers a range of practical advantages, including reduced noise at low light levels [1, 3, 8]. In this approach, single-photon wave packets that are transmitted through an object are detected by a simple bucket detector that only counts the photons but does not distinguish their position or momentum state. Then, an object can be imaged by preparing the incident photons with wavefunctions $\Psi_N(z)$ centered at different spatial positions z_N , as sketched on the left side of Fig. 1. A characteristic single-photon wavefunction can be approximated with a Gaussian shape with the width σ_z ,

$$\Psi_N(z) = \frac{1}{(2\pi\sigma_z^2)^{1/4}} \exp\left(-\frac{(z - z_N)^2}{4\sigma_z^2}\right). \quad (1)$$

After the photons propagate through the phase object, their wavefunctions exhibit the corresponding phase modulations $O(z) = e^{i\phi(z)}$, however the norm of the wavefunction $|\Psi_N(z)|^2$ and thereby the photon rate do not change.

To detect the influence of the phase object, we suggest to position in the photon path a specially designed and tilted Si metasurface, which features a linear optical transfer function (OTF)

$$H(k_z^{(s)}) = ak_z^{(s)} + b, \quad (2)$$

in the transverse momentum space k_z , where a and b are constant coefficients. As established in classical optics regime, such a metasurface can effectively perform the wavefront differentiation in

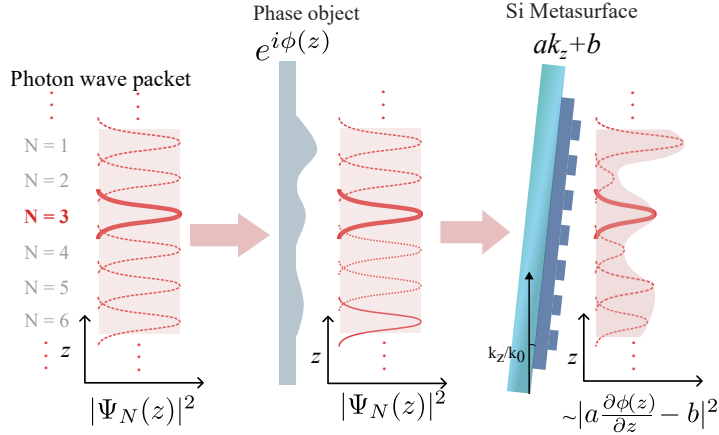


Fig. 1. **Schematic diagram of phase-gradient imaging using quantum light.** (Left) Single-photon wave packets $\Psi_N(z)$ are prepared at different spatial positions labeled $N = 1, 2, 3, \dots$ in the transverse direction z . Each wavepacket has a finite width with Gaussian-like shape of the wavefunction norm $|\Psi_N(z)|^2$, as indicated by lines. (Middle) After propagating through a phase object, the wavepackets acquire a spatially varying phase $\phi(z)$, while their probability amplitude remains unchanged. (Right) The Si metasurface imposes a linear optical transfer function $(ak_z + b)$ on the wavefunction in k_z -space, equivalent to taking a spatial derivative of phase in real space, see an expression under the plot. Consequently, the phase variation encoded in the quantum state is converted into measurable photon rate modulation, allowing direct extraction of the phase gradient at the single-photon level.

the z direction [25, 40, 41]. However, the operation needs to be specially analyzed and optimized in the quantum regime. The detectable photon rate can be estimated as (see Supplementary Sec. S2 for the derivation details)

$$C_N(z) = \int dz \left| \mathcal{F}_z^{-1} \left[H(k_z) \mathcal{F}_z [O(z) \Psi_N(z)] \right] \right|^2 \propto \left[\frac{a^2}{4\sigma_z^2} + \left(a \frac{\partial \phi(z)}{\partial z} - b \right)^2 \right]_{z=z_N} \quad (3)$$

where \mathcal{F}_z indicates the Fourier transform along the z -direction. The nonzero constant b is related to the metasurface tilt, which introduces an asymmetry into the quadratic phase gradient term and permits distinguishing the positive and negative phase gradients for the unambiguous reconstruction of phase modulations.

We note that to perform accurate phase gradient extraction, the Fourier spectrum of the photon wavefunction must lie entirely within the approximately linear region of the OTF of the width Δk , i.e. we require that $\sigma_z \geq 2/\Delta k_z$. This conditions sets the lower limit on the spatial resolution, since the object phase gradient is effectively averaged over the σ_z width of the photon wavepacket. This is consistent with the resolution limit in the classical case, being also inversely proportional to Δk according to the Fourier transform properties.

2.2. Nonlinear metasurface for photon-pair generation

In order to prepare the required single-photon states $\Psi_N(z)$ for object imaging, we employ the momentum correlations between two photons generated through the process of spontaneous parametric down-conversion (SPDC) according to the quantum ghost imaging scheme. In traditional setups, bulk nonlinear crystals were used for SPDC-based generation of entangled photons [3, 8]. Instead, we employ a photon-pair source based on a compact nonlinear metasurface

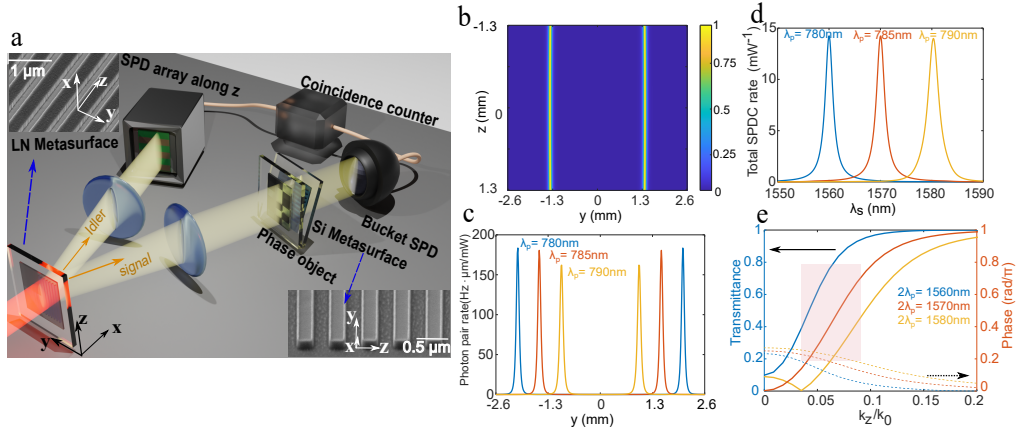


Fig. 2. Concept of metasurface system for quantum phase-gradient imaging with simulated features. **a.** The sketch of the setup. The transverse directions are z and y . The SEM image of the LiNbO_3 metasurface is shown in the top-left corner, and that of the Si metasurface is shown at the bottom-right corner. The phase object is prepared with a spatial light modulator (SLM). The Si metasurface is placed immediately after the object with a slight tilt to produce a linear OTF. **b.** The photon-pair emission pattern from LiNbO_3 with anti-symmetric uniform z -direction distribution and narrow y -direction distribution. The wavefield propagation direction is set to the x -direction. **c.** The tunable emission along the y -direction. Tuning the pump wavelength shifts the SPDC emission along the y -axis, which is used for object imaging in this direction. **d.** The spectrum of the metasurface-based SPDC process for three selected pump wavelengths. The bandwidth of the generated photons is around 3nm. **e.** The optical transfer function produced by the Si metasurface resonates at 1570nm. The solid lines show the amplitude transfer function with respect to incident angles into the metasurface across the three central signal wavelengths. The dashed lines show the phase modulation function through the metasurface. The shaded box marks the almost linear region applied in the experiment.

that was recently used to realize ghost imaging of amplitude objects, offering a potential to increase the number of resolution cells by several orders of magnitude [38].

Accordingly, we propose a complete metasurface-based quantum phase gradient imaging system, as illustrated in Fig. 2a. Pairs of photons are generated through SPDC from a metasurface incorporating quadratically nonlinear LiNbO_3 layer. The LiNbO_3 metasurface is designed by leveraging nonlocal guided-mode resonances (GMRs) in a lithium niobate thin film, where a SiO_2 grating deposited on top mediates resonant coupling between the free-space radiation and the guided modes [33]. A scanning electron microscope (SEM) image of the fabricated LiNbO_3 metasurface is shown in Fig. 2a. It consists of a sub-wavelength-scale silica grating with a thickness of 200 nm on top of a 300 nm thick x -cut LiNbO_3 thin film. The grating period was chosen to be 900 nm with a width of 500 nm. The simulation details for the design can be found in Supplementary Sec. S1.1. The design ensures that the nonlinear interactions are resonantly enhanced at the photon wavelengths, increasing the signal and idler generation through SPDC.

Due to the conservation of transverse momentum, the signal and idler photons are emitted at opposite angles, and we separately focus them by lenses. In the image plane of idler photons, we position a 1D array of single-photon detectors along the z direction, whereas a phase object is placed in the image plane of signal photons. In these planes, the photon emission is broad in z , but narrow in y direction, as shown in Fig. 2b. The photons are anti-correlated in z , allowing for ghost imaging, since a detection of idler photon at a particular z_i position heralds the signal

photon incidence on the object at the position $z_s \simeq -z_i$ [38]. We can thereby perform phase gradient imaging according to the ghost imaging concept discussed in the previous Sec. 2.1 and sketched in Fig. 1, with $z_N \simeq -z_i$.

In the orthogonal y -direction, we perform the imaging by all-optically scanning the photon positions by tuning the pump wavelength [38, 39]. The resonant photon wavelength shifts almost linearly with the incident angle, and this angular dispersion enables a linearly tunable emission angle for the generated photon pairs, ranging from $\lambda_{s,i} = 1560$ nm to 1580 nm, for the pump laser wavelengths from 780 nm to 790 nm, as illustrated in Fig. 2c. Importantly, the photon rate is consistently enhanced across all these wavelengths, with the photon bandwidth indicating the metasurface quality factor $Q_{LN} \cong 500$ according to Fig. 2d. The resolution along the y -axis is further influenced by the spectral bandwidth (Fig. 2d) used in the scanning protocol. The minimum resolvable pixel size along y -direction is determined by the condition that cross-talk is small, ensuring reliable phase-gradient extraction. In Sec. 2.5, we evaluate these resolution limits through simulations under experimental conditions (see also simulation details in Sec. S3 of the supplementary material).

Overall, the spatial correlation between the paths of signal and idler photons governs the coincidence at each pixel on the 1D detector array along the z -direction, with the y -coordinate determined by the pump wavelength. In this way, we can acquire a two-dimensional spatial profile of the object phase-gradient $\partial\phi/\partial z$.

2.3. Design of Si metasurface for phase gradient imaging

We now discuss the design principles of a silicon metasurface that is placed after the phase object to facilitate the gradient imaging, as sketched in Fig. 1. Ideally, its optical transfer function should follow Eq. (2). Additionally, this response should be sustained over a range of photon wavelengths, that is required to perform the imaging scanning in the y -direction as illustrated in Figs. 2c,d. This is a highly nontrivial requirement, in contrast to previous structures that we optimised for single-wavelength operation under classical continuous laser illumination [24].

We design the metasurface in the form of a periodic Si grating on a Si waveguide layer above a SiO_2 substrate. Part of the incident light excites waveguide modes that propagate laterally, interfere, and re-radiate, while another portion is directly transmitted. The interference between the diffracted and directly transmitted field allows one to create a tailored transmission spectrum of selective spatial frequency [42]. The period of the grating is determined by the working wavelength. Given the resonant photon wavelength λ , the grating period can be found as $d = \lambda/n_e$, where n_e is the effective mode index, and we consider first-order resonance with the normally incident plane wave. As mentioned above, the Si metasurface must also operate over the photon bandwidth to cover all the scanning wavelengths (1560 to 1580 nm), while simultaneously providing a linear transfer function with sufficient slope for high sensitivity with a wide enough range $k_t \pm \Delta k_z/2$ to maximize the spatial resolution, where k_t corresponds to a fixed tilting angle of the metasurface. This requires a certain balance between the quality factor (Q_{si}) and the mode dispersion, which can be achieved by adjusting the grating duty cycle l , since $Q_{si} \propto 1/\sin^2(l\pi)$. We therefore performed parametric sweeps over l to optimize the design. With a 100 nm thick Si thin film and 120 nm grating height, a grating period 615 nm and duty cycle of 0.45 results in a quality factor $Q_{si} \cong 20$. More details on the design procedure are provided in Sec. S1.2 of the Supplementary material. In this design, the tilting angle of the metasurface $\theta_t = 4^\circ$. Most importantly, the combined effect of the grating and thin film allows the OTF to retain a linear form over the tunable wavelength range. Indeed, in the range $\Delta k_z = 0.05$, the slope of the linear OTF for all three photon wavelengths shown in the shaded part of Fig. 2e (from 1560 to 1580 nm) is very similar, $a \cong 11.6, 12, 12.8$ (unitless in k_z/k_0 plot). The constant term is, for a tilted metasurface, $b \cong 0.4, 0.5, 0.7$. The wavelength dependence of a and b can be fully taken into account allowing for accurate phase gradient reconstruction, as we discuss in the following.

2.4. Experimental characterization of the metasurfaces

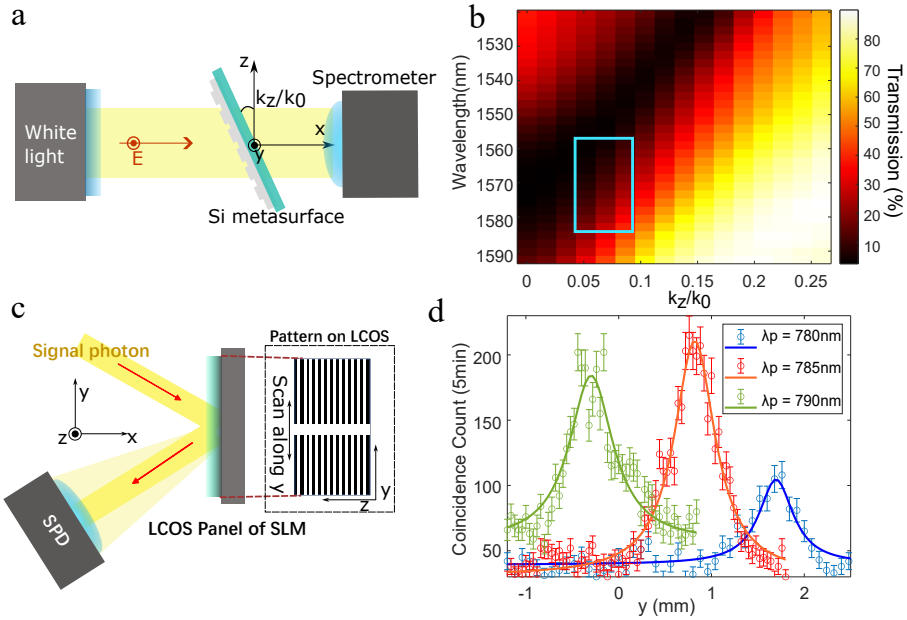


Fig. 3. **a**. A transmission setup used to experimentally check the incident-angle dependent transmission of the Si metasurface by rotating the metasurface around the y -axis. The incident wave is y -polarised. **b**. The experimental transmission of the Si metasurface. The blue box marks the applicable region for phase-gradient imaging. **c**. A pattern formed with an unmodulated part and a highly reflective part is projected on the LCOS panel of the SLM. By shifting the pattern along the y -direction, we can subsequently locate the beam spot for each wavelength. **d**. Experimentally extracted beam locations on the LCOS panel. Each data point is integrated for 5 minutes.

We now perform the separate experimental characterization of linear and nonlinear metasurfaces, before their integration in a phase-gradient imaging system.

By design, a linear transmission through the Si metasurface should depend on the incident wavevector along the z -direction. This dispersion is measured through a transmission setup with y -polarised white light and the Si metasurface being mechanically rotated, as sketched in Fig. 3a. We indeed observe a linear OTF in the marked blue box of the experimentally measured transmission in Fig. 3b. It corresponds to the shaded region in the theoretically calculated Fig. 2e, which is suitable for phase-gradient imaging.

Next, we determine the spatial coordinates along the y direction of the signal photons emitted from the LiNbO_3 metasurface, at the three selected pump wavelength of 780, 785, and 790 nm, which were theoretically modeled in Figs. 2c-d. For this purpose, we project the signal photons on the liquid crystal on silicon (LCOS) panel, and employ a hybrid test phase-modulation pattern that comprises two distinct regions, as sketched in Fig. 3c. One is a non-diffractive section spanning around 0.6 mm in the y -direction, which preserves the incident beam wavefront. The other is a heavily diffractive region that imposes strong spatial phase modulation over the rest of the area. By shifting the pattern along the y -axis using the HOLOEYE Pattern Generator software, the spatial overlap between the non-diffractive section and the transverse profile of the signal photon was systematically varied. Such variation was quantified by monitoring the coincidence count rate. A maximum in the coincidence count occurs when the non-diffractive region aligns with the center of the signal photon beam, as this configuration minimizes diffraction-induced

losses. Consequently, the y -coordinate of the beam center for each wavelength was identified by tracking the peak in the coincidence count rate as a function of the pattern's positional shift. The results presented in Fig. 3d show that the signal photons have spatially resolved positions in the y -direction. Whereas the photon distributions are wider compared to the theoretical prediction in Fig. 2c resulting in a small overlap, this still allows for the accurate determination of independent phase-gradients along z at these locations, as we demonstrate in the following. Whereas we experimentally realize 3-pixel resolution in the y direction, corresponding to the three pump wavelengths, we discuss in the following section the theoretical potential for significantly enhanced imaging resolution.

2.5. Theoretical analysis of the phase-gradient imaging resolution

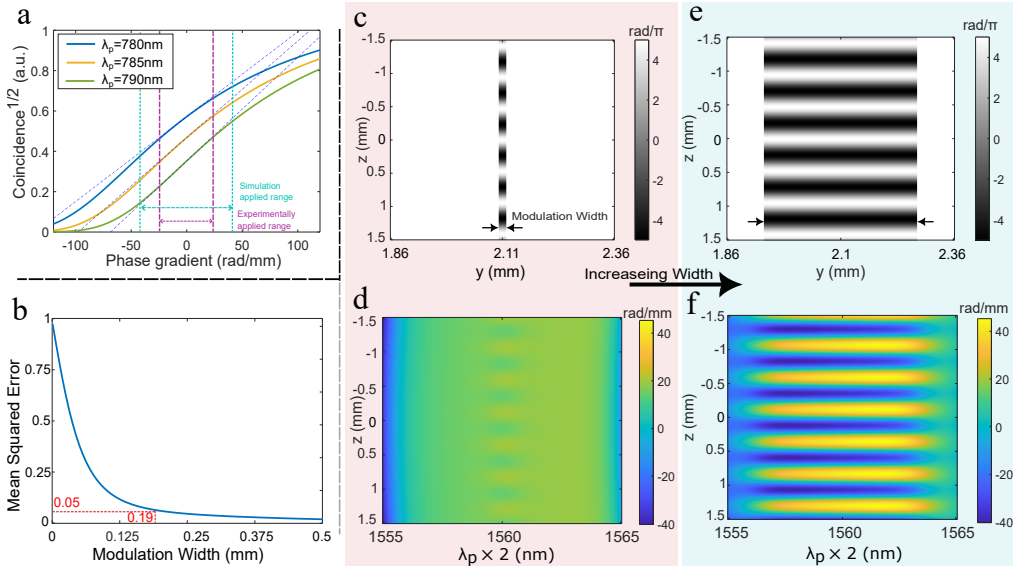


Fig. 4. Resolution of quantum phase-gradient imaging. **a.** The simulated relation between the square root of photon coincidence rate and the phase gradient $\partial\phi/\partial z$ at different pump wavelengths. The coincidences are normalised with respect to the object- and Si-metamaterial-free coincidence rate. The dash lines are the linear fitting around the zero phase gradient. Labels indicate the maximum resolvable phase gradients. **b.** The average deviation of the simulated reconstructed phase gradient from the target phase gradient at $2\lambda_p = 1560$ vs. the phase modulation width along y . The dashed line marks the 5 % error relative to the target phase gradient. **c,d.** The input cosine phase modulation patterns with modulation width of (c) 0.02 mm and (e) 0.35 mm. **d,f.** The phase gradient reconstruction simulated by scanning through $\lambda_p \times 2 = 1555$ to 1565 nm for the patterns shown in (c) and (e), respectively.

Using the designed metasurfaces and the simulated optical transfer function (OTF), we theoretically analyze the imaging resolution. Since the linear part of the OTF spans a limited k -space region as shown in the shaded part of Fig. 2e, the metasurface can accurately resolve only a specific range of phase gradients. Under our experimental conditions, the photon wavefunction width is $\sigma_z \simeq 87\mu\text{m}$, and we find that the term $a^2/(4\sigma_z^2)$ is much smaller than the second bracket on the right of Eq. (2), see details in the Supplementary Sec. S2.1. Then, we perform the exact calculations based on the Fourier transforms according to Eq. (2), and analyze whether the square root of photon counts matches the theoretically expected linear dependence on $a\partial\phi/\partial z - b$. The results presented in Fig. 4a indicate that the designed metasurface can resolve a maximum

phase gradient of approximately ± 40 rad/mm across 1570 ± 10 nm wavelength range when the metasurface is tilted by 4° or $k_z/k_0 \simeq 0.07$, and ± 25 rad/mm with high precision of linear correspondence for any wavelength within this range. On the other hand, the maximum number of spatially resolvable object pixels along the z -direction is governed by the general principles of ghost imaging, being approximately proportional to the pump beam diameter and the associated nonlinear metasurface dimensions [38].

The spatial resolution of phase-gradient imaging along the y -direction, analogous to amplitude imaging, is directly governed by the width of spatial emission along the y -direction [38], which is proportional to the quality factor Q_{LN} . Consequently, the overall resolution of the system can be significantly enhanced by increasing the nonlinear metasurface size and the quality factor of nonlocal resonances at the photon wavelengths.

We aim to extract the phase gradient along the z direction. However, since the measurements are effectively spatially averaged over the photon wavefunction, it is important to check that the gradient reconstruction is not affected by phase variations in the orthogonal (y) direction. To quantitatively this aspect, we performed numerical simulations for the photon emission spectrum centered at 1560 nm. We considered a phase modulation with a cosine profile was applied along the z -direction with varying width across the y -coordinate, while the outside area has no phase modulation, as shown in Figs. 4c,e. The calculated example phase gradient patterns by the combined ghost imaging and scanning are shown in Fig. 4d,f. We evaluated the difference between the numerically reconstructed phase gradient $F_s(z, w_m)$ and designed phase gradient $F_t(z) = \partial\phi(z)/\partial z$ by the mean squared error [43],

$$\text{Err}(w_m) = \left| \int_{z_{\min}}^{z_{\max}} |F_t(z) - F_s(z, w_m)|^2 dz \right| \Big/ \int_{z_{\min}}^{z_{\max}} |F_t(z)|^2 dz, \quad (4)$$

where w_m is the modulation width. The results in Fig. 4b demonstrate a decrease in the overall error as the modulation width expanded as from Fig. 4c to Fig. 4e. Notably, the phase gradient retained 95% of its designed phase gradient when the minimum resolvable feature size along the y -direction is greater than 0.18 mm, which corresponds to a spectral bandwidth of approximately 3 nm. This observation aligns with the theoretical prediction derived from the nearly linear dispersion relationship between the pump wavelength and the emission center's spatial shift along y , which is intrinsically linked to the system's spectral waist. The consistency between the empirical resolution limit (3 nm) and the spectral waist further corroborates the role of bandwidth in constraining phase-gradient imaging resolution, which agrees with the conclusion from the amplitude imaging.

2.6. Experimental quantum phase ghost imaging

After determining the pixel positions and theoretically predicting the resolution limit, two 6×3 -pixel patterns were projected onto the LCOS panel. Each pixel has a size $\Delta y \times \Delta z = 800\mu\text{m} \times 350\mu\text{m}$. Photon coincidence data for each pixel were accumulated over a 1-hour integration period, with measurements recorded at 5-minute intervals to yield 12 data points per pixel. This sampling strategy enabled robust error analysis demonstrated in Sec. S5 in supplementary material and confirmed the shot-noise limited error. Both the T-shaped (Fig. 5a) and S-shaped (Fig. 6a) patterns were formed by sections of linear phase function along z -direction and were designed with a maximum phase gradient of 25 rad/mm, consistent with the calculated upper limit of high fidelity resolvable phase gradients. The correlation width of the photon pair along the z -direction is $\sigma_z = 87 \mu\text{m}$, resulting in a negligible first term in Eq. 3 compared to the second term for phase gradient reconstruction.

As the pattern size along the z -axis approaches the limit defined by the device's collection angle, a clear Gaussian distribution of collection efficiency is observed in both the z - and y -coordinates. Therefore, in the reconstruction of the phase gradient image, we use one object as calibration

object and perform a fitting to the coincidence-to-phase-gradient relation with additional Gaussian collection efficiency function. The fitter parameters are later applied for direct reconstruction of another object. To be more specific, experimentally, the detected coincidence function along z is given by,

$$\tilde{C}(z) = G(z)C(z) \quad (5)$$

where $C(z)$ is the coincidence function Eq.3 at a fixed pump wavelength λ_p , and $G(z)$ is a Gaussian function with center position β_{λ_c} and width γ_{λ_c} at a y -pixel corresponding to the center wavelength $\lambda_c := 2\lambda_p$,

$$G(z) = \exp\left(-\beta_{\lambda_c}^2(z - \gamma_{\lambda_c})^2\right). \quad (6)$$

To extract the data and reconstruct the phase gradient, we employ a fitting procedure using target functions $\tilde{f}(C(z))$. The fitting functions consist of an inverse Gaussian function combined with a linear scaling function, which together facilitate the conversion of coincidence counts into phase gradient values.

$$\tilde{f}(C(z)) = \alpha_{\lambda_c} \sqrt{\frac{C(z)}{G(z)}} + \delta_{\lambda_c} = \alpha_{\lambda_c} \sqrt{C(z)_{eff}} + \delta_{\lambda_c} \quad (7)$$

where $\alpha_{\lambda_c}, \beta_{\lambda_c}, \gamma_{\lambda_c}, \delta_{\lambda_c}$ are the set of fitting parameters corresponding to different signal central wavelength. $C(z)_{eff}$ denotes the rescaled effective coincidence function for fixed wavelength. Based on the theoretical resolution limit analysis and the different collection efficiency along the y -coordinate, all four fitting parameters α_{λ_c} and δ_{λ_c} must also be treated separately for each wavelength. In our case, we perform fitting individually for all three wavelengths along y $\lambda_c := 2\lambda_p \in \{1560, 1570, 1580\}$ (nm) and the coincidence data of six pixels along z , $z = 1, \dots, 6$, generates the fitting function.

We applied the function $\tilde{f}(C(z))$ to the coincidence data obtained from the T-shaped object (Fig. 5c), using a theoretical phase gradient target $F_t(z)$ as a fitting reference (Fig. 5a). From this process, the fitting parameters were extracted by minimizing the objective function $\tilde{f}(C(z)) - F_t(z)$, that is $\min(\tilde{f}(C_z, \lambda_c) - F_t(z, \lambda_c)) \mapsto (\alpha_{\lambda_c}, \beta_{\lambda_c}, \gamma_{\lambda_c}, \delta_{\lambda_c})$. The fitted Gaussian background function is shown in Fig. 5d. As we apply the inverse Gaussian function in Fig. 5c, at the pixel location $(z, \lambda_c = 2\lambda_p) = (4, 1560)$, a low coincidence count was observed due to random error, compounded by an inherently low coincidence count at $2\lambda_p = 1560$ nm, as illustrated in Fig. 3b. However, despite this outlier, the remaining five precise data points allowed for the accurate extraction of the four fitting parameters when the T-shaped object was used for calibration (see Supplementary). Furthermore, we verified the fitted results by reconstructing the rescaled coincidence data into an inverse Gaussian distribution, revealing an almost linear relationship between the fitted and original data. An example at $2\lambda_p = 1580$ nm is shown in Fig. 5f.

The extracted fitting parameters were then applied to $\tilde{f}(C_z)$ with C_z as the raw coincidence data measured from the S-shaped object (Fig. 6), enabling the reconstruction of its phase gradient. By comparing the target phase gradient in Fig. 6b and the reconstructed phase gradient Fig 6c via the mode overlap method [44, 45], it demonstrates an 88% image similarity. The same approach can also be implemented in reverse. In Sec. S4 of supplementary material, we include the reconstruction from calibration of an S-shaped object to a T-shaped object.

3. Discussion

By combining these two key functions into one nanophotonic platform, the system reaches a level of compactness and integration that has never been seen in quantum imaging setups. This dual-role metasurface method not only shrinks the physical size to the millimeter scale but also removes the alignment issues common in multi-element bulk-optical systems.

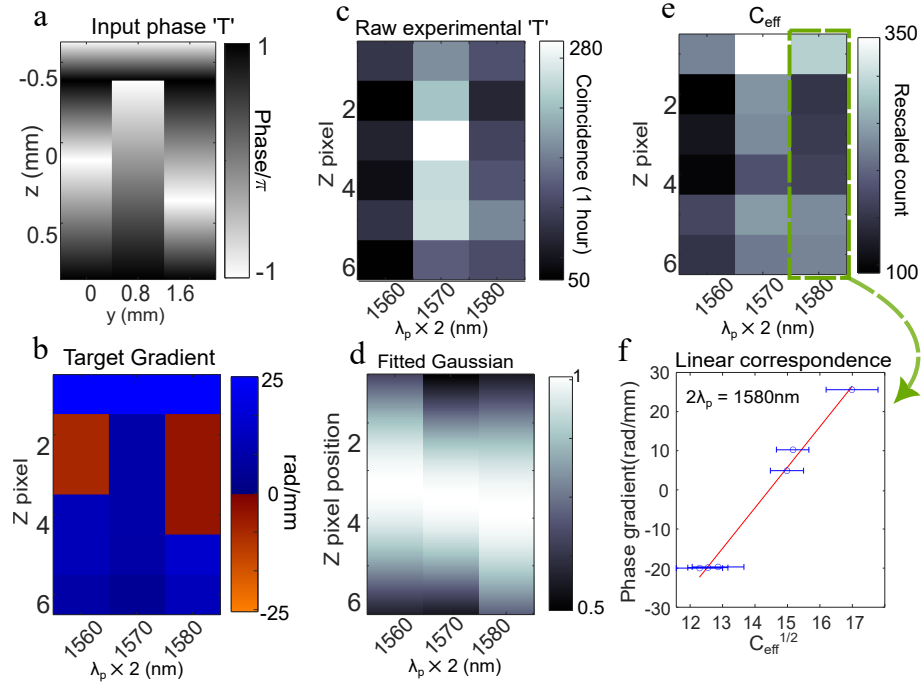


Fig. 5. Calibration for phase gradient image reconstruction. **a.** The projected T-shaped phase object form by multiple sections of linear phase modulation along z -axis. **b.** The corresponding target phase gradient of Fig. 5a derived as $\partial\phi(z)/\partial z$. **c.** The experimental shot noise-limited coincidence count data of the T-shaped phase modulation pattern before processing. **d.** The Gaussian functions $G(z)$ are fitted from objective function minimization with normalization. **e.** The Rescaled coincidence C_{eff} by the quotient of the Gaussian background in Fig. 5c. **f.** The rescaled coincidence data at $\lambda c = 2\lambda_p = 1580\text{nm}$ and the target phase gradient show a linear relation. The coincidence of the other two wavelengths is fitted individually.

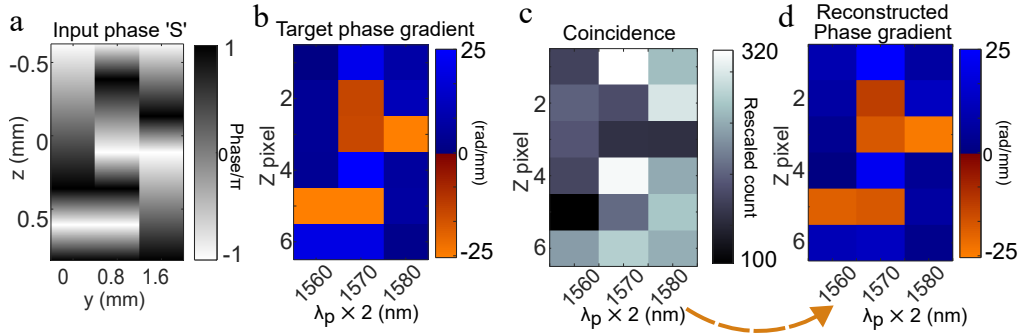


Fig. 6. Proof-of-principle demonstration of quantum phase-gradient imaging. **a.** The input S-shaped phase modulation. **b.** The theoretical phase gradient of the S pattern. **c.** The rescaled coincidence data C_{eff} by removing the fitted Gaussian background in Fig. 5d. **d.** The reconstructed phase gradient of S-shaped phase pattern via further apply linear fitting parameters for each wave length Fig. 5.

A key strength of our configuration is its large field of view combined with inherent all-optical

tunability in quantum light generation. This tunability, along with the spatial mode control provided by the LiNbO_3 metasurface, allows the system to easily adjust to various imaging targets and operational conditions. This includes biological specimens and larger structured objects. Meanwhile, associated with the precisely engineered Si metasurface with low Q_{si} for a larger bandwidth phase filter, the phase response can be reconfigured quickly and seamlessly, without the need for mechanical adjustments or electronic feedback.

The current setup solution can be improved in simple ways. First, increasing the diameter of the LiNbO_3 metasurface would allow it to capture and control higher spatial frequency components of the two-photon field. Second, shaping the pump beam so that it is flatter and more uniform across the metasurface aperture would further enhance performance. Both adjustments broaden the correlation bandwidth in momentum space, which ultimately sharpens the precision of axial and transverse phase gradient measurements.

A particularly notable aspect of this protocol is that it achieves phase gradient extraction without the need for an interferometer or any direct interference measurements. Instead, the phase information is embedded in engineered two-photon correlations, shaped entirely by the metasurface. This design eliminates the stringent stability requirements and vulnerability to environmental noise that often constrain interferometer-based quantum phase imaging, resulting in a simpler experimental setup and greater robustness for real-world applications.

Furthermore, we demonstrate that positioning the metasurface for phase gradient extraction directly after the phase object still delivers phase retrieval precision well within acceptable limits for most practical uses. This means that relay optics or telescopic beam expansion are not strictly required, further enhancing the system's compactness. For general-purpose imaging, the capability to perform quantum phase measurements without long free-space propagation stages marks an important step toward truly portable and field-deployable quantum sensors.

Taken together, the system shows that integrating metasurfaces can fundamentally expand the design possibilities for quantum imaging systems. By uniting photon-pair generation, state manipulation, and phase retrieval within a single class of nanostructured components, this approach paves the way for scalable, multi-functional quantum optical devices—free from the size and complexity constraints of traditional bulk optics.

4. Conclusion

In this study, we have developed a compact and versatile quantum phase-gradient imaging system that builds upon previous work in quantum imaging using a LiNbO_3 metasurface as an entangled photon source. While the LiNbO_3 metasurface has been instrumental in generating spatially entangled photon pairs for quantum imaging with a combined ghost imaging and all-optical scanning protocol, this work extends its application by integrating a silicon (Si) metasurface for phase gradient extraction, marking the first demonstration of metasurfaces being used for both generation and detection in a quantum imaging system.

The compact design of the system is a key innovation, enabled by the use of nonlocal metasurfaces that provide precise control over photon interactions. The Si metasurface, in particular, plays a critical role in extracting phase gradients through its linear optical transfer function (OTF), allowing for the reconstruction of phase information with spatial quantum correlation. This approach not only simplifies the optical setup but also enhances the system's portability, making it suitable for applications where space and efficiency are paramount. Another notable feature of the system is its switchable operation between quantum amplitude imaging and phase-gradient imaging.

Our experimental results validate the theoretical framework, showing that the system can resolve phase gradients up to 25 rad/mm with high fidelity. The proof-of-principle experiment with calibration-based reconstruction method achieve an 88% similarity. This lays the groundwork for further optimization, including improvements in resolution and contrast through

advanced fabrication techniques and enhanced quality factors of LiNbO₃.

In conclusion, this work establishes a new paradigm for compact and switchable quantum phase-gradient imaging, leveraging the dual functionality of metasurfaces. The integration of generation and detection within a single platform opens up exciting possibilities for applications in quantum imaging, sensing, biomedical metrology, and beyond. In particular, application to fast all optical transparent/phase-only object tracking could associate LiDAR to achieve higher precision in a complex environment.

5. Methods

The experimental setup is detailed as follows. A tunable pump laser for spontaneous parametric down-conversion (SPDC) (FPL785P, Thorlabs) operates within a wavelength range of 779 nm to 791 nm. The laser beam is passed through a 200 mm focal length lens and an 850 nm short-pass filter before being projected onto the LiNbO₃ metasurface. The beam is focused to a waist of 200 μ m on the metasurface, which is mounted on a 3D translation stage for precise positioning. A 50 mm lens is then used to collimate the light.

The photons generated through SPDC are initially z-polarized. To convert them into y-polarization for compatibility with the Si metasurface, a half-wave plate oriented at 45 degrees is employed before the signal and idler beams are separated. A dichroic mirror (D-mirror) is used to split the signal and idler photons after passing through a band-pass filter centered at 1570 nm with a bandwidth of ± 50 nm.

One optical path includes a scanning slit moving along z, which mimics a 1D detector array, while the other path incorporates the SLM (PLUTO 2.1, HOLOEYE) to produce the phase pattern, followed by the Si metasurface. The Si metasurface and the scanning slit are positioned at equal distances from the D-shaped mirror to ensure high-precision correlation measurements. Due to the broad scanning bandwidth, the photons are directed to single-photon detectors based on InGaAs/InP avalanche photodiodes (ID230, ID Quantique) via multimode fibers. Before being coupled into the fibers, photons from both paths pass through a band-pass filter centered at 1570 nm with a bandwidth of ± 30 nm to ensure high-quality quantum measurements.

Coincidence events are characterized using a time-to-digital converter (ID801, ID Quantique), with the coincidence window set to 0.42 ns for precise timing correlation analysis.

6. Fabrication

The silicon gratings were fabricated using electron beam lithography (EBL) combined with reactive ion etching (RIE). First, commercially available amorphous silicon thin films on glass substrates (Tafelmaier Dünnenschicht Technik GmbH) were cleaned in a cleaning machine (OPTIwet SB 30). The silicon thickness was adjusted to the target value by argon-ion beam etching, followed by the deposition of a conductive chromium layer and a 100 nm negative electron-beam resist (EN038, Tokyo Ohka Kogyo Co., Ltd.). The resist was then patterned using a variable-shaped beam electron-beam lithography system (Vistec SB 350).

After exposure, the resist was developed in a developer (OPD 4262), and the pattern was transferred to the chromium layer by ion beam etching (Oxford Ionfab 300). The underlying silicon layer was then etched to the desired trench depth using reactive ion etching (RIE-ICP, Sentech SI-500 C). Finally, the residual resist and chromium layer were removed in acetone and a ceric ammonium nitrate-based solution, respectively.

7. Acknowledgment

This work was supported by the Australian Research Council (<https://doi.org/10.13039/501100000923>) Centre of Excellence for Transformative Meta-Optical Systems - TMOS

(CE200100010) and the Deutsche Forschungsgemeinschaft (DFG, German Research Foundation) project Meta Active IRTG 2675 (437527638).

8. Disclosures

The authors declare no conflicts of interest.

References

- [1] T. B. Pittman, Y. H. Shih, D. V. Strekalov, and A. V. Sergienko, “Optical imaging by means of 2-photon quantum entanglement”, *Phys. Rev. A* **52**, R3429–R3432 (1995) 10.1103/PhysRevA.52.R3429.
- [2] Y. Shih, “Quantum Imaging”, *IEEE J. Sel. Top. Quantum Electron.* **13**, 1016–1030 (2007) 10.1109/JSTQE.2007.902724.
- [3] M. J. Padgett and R. W. Boyd, “An introduction to ghost imaging: quantum and classical”, *Philos. Trans. R. Soc. A* **375**, 20160233 (2017) 10.1098/rsta.2016.0233.
- [4] P.-A. Moreau, E. Toninelli, T. Gregory, and M. J. Padgett, “Imaging with quantum states of light”, *Nat. Rev. Phys.* **1**, 367–380 (2019) 10.1038/s42254-019-0056-0.
- [5] M. Gilaberte Basset, F. Setzpfandt, F. Steinlechner, E. Beckert, T. Pertsch, and M. Gräfe, “Perspectives for Applications of Quantum Imaging”, *Laser & Photonics Rev.* **13**, 1900097 (2019) 10.1002/lpor.201900097.
- [6] P. Cameron, B. Courme, D. Faccio, and H. Defienne, “Shaping the spatial correlations of entangled photon pairs”, *J. Phys. Phot.* **6**, 033001 (2024) 10.1088/2515-7647/ad50b1.
- [7] H. Defienne, W. P. Bowen, M. Chekhova, G. B. Lemos, D. Oron, S. Ramelow, N. Treps, and D. Faccio, “Advances in quantum imaging”, *Nat. Photon.* **18**, 1024–1036 (2024) 10.1038/s41566-024-01516-w.
- [8] A. Forbes and F. Nothlawa, “How a thirty-year-old quantum tale of two photons became ghost imaging”, *Commun. Phys.* **8**, 174 (2025) 10.1038/s42005-025-02099-w.
- [9] G. Brida, M. Genovese, and I. Ruo Berchera, “Experimental realization of sub-shot-noise quantum imaging”, *Nat. Photonics* **4**, 227–230 (2010) 10.1038/nphoton.2010.29.
- [10] N. Samantaray, I. Ruo-Berchera, A. Meda, and M. Genovese, “Realization of the first sub-shot-noise wide field microscope”, *Light. Sci. & Appl.* **6**, e17005–e17005 (2017) 10.1038/lsa.2017.5.
- [11] C. M. Caves, “Quantum-mechanical noise in an interferometer”, *Phys. Rev. D* **23**, 1693–1708 (1981) 10.1103/PhysRevD.23.1693.
- [12] D. Rusca and N. Gisin, *Quantum cryptography: an overview of quantum key distribution*, 2024, <https://arxiv.org/abs/2411.04044>.
- [13] G. B. Lemos, V. Borish, G. D. Cole, S. Ramelow, R. Lapkiewicz, and A. Zeilinger, “Quantum imaging with undetected photons”, *Nature* **512**, 409–U382 (2014) 10.1038/nature13586.
- [14] A. V. Paterova, H. Z. Yang, C. W. An, D. A. Kalashnikov, and L. A. Krivitsky, “Tunable optical coherence tomography in the infrared range using visible photons”, *Quantum Sci. Technol.* **3**, 025008 (2018) 10.1088/2058-9565/aab567.
- [15] V. Giovannetti, S. Lloyd, and L. Maccone, “Advances in quantum metrology”, *Nat. Photonics* **5**, 222–229 (2011) 10.1038/nphoton.2011.35.

- [16] G. Ortolano, A. Paniate, P. Boucher, C. Napoli, S. Soman, S. F. Pereira, I. Ruo-Berchera, and M. Genovese, “Quantum enhanced non-interferometric quantitative phase imaging”, *Light. Sci. & Appl.* **12**, 171 (2023) 10.1038/s41377-023-01215-1.
- [17] T. L. Nguyen, S. Pradeep, R. L. Judson-Torres, J. Reed, M. A. Teitell, and T. A. Zangle, “Quantitative phase imaging: recent advances and expanding potential in biomedicine”, *ACS Nano* **16**, 11516–11544 (2022) 10.1021/acsnano.1c11507.
- [18] J. R. Fienup, “Phase retrieval algorithms: a personal tour [invited]”, *Appl. Opt.* **52**, 45 (2013) 10.1364/AO.52.000045.
- [19] Y. Park, C. Depeursinge, and G. Popescu, “Quantitative phase imaging in biomedicine”, *Nat. Photonics* **12**, 578–589 (2018) 10.1038/s41566-018-0253-x.
- [20] F. Zernike, “Phase contrast, a new method for the microscopic observation of transparent objects part ii”, *Physica* **9**, 974–986 (1942) 10.1016/S0031-8914(42)80079-8.
- [21] A. Silva, F. Monticone, G. Castaldi, V. Galdi, A. Alù, and N. Engheta, “Performing mathematical operations with metamaterials”, *Science* **343**, 160–163 (2014) 10.1126/science.1242818.
- [22] T. Zhu, Y. Zhou, Y. Lou, H. Ye, M. Qiu, Z. Ruan, and S. Fan, “Plasmonic computing of spatial differentiation”, *Nat Commun* **8**, 15391 (2017) 10.1038/ncomms15391.
- [23] H. Kwon, E. Arbabi, S. M. Kamali, M. Faraji-Dana, and A. Faraon, “Single-shot quantitative phase gradient microscopy using a system of multifunctional metasurfaces”, *Nat. Photonics* **14**, 109–114 (2020) 10.1038/s41566-019-0536-x.
- [24] L. Wesemann, J. Rickett, J. C. Song, J. Q. Lou, E. Hinde, T. J. Davis, and A. Roberts, “Nanophotonics enhanced coverslip for phase imaging in biology”, *Light Sci. Appl.* **10**, 98 (2021) 10.1038/s41377-021-00540-7.
- [25] L. Wesemann, T. J. Davis, and A. Roberts, “Meta-optical and thin film devices for all-optical information processing”, *Appl. Phys. Rev.* **8**, 31309 (2021) 10.1063/5.0048758.
- [26] A. Ji, J.-H. Song, Q. Li, F. Xu, C.-T. Tsai, R. C. Tiberio, B. Cui, P. Lalanne, P. G. Kik, D. A. B. Miller, and M. L. Brongersma, “Quantitative phase contrast imaging with a nonlocal angle-selective metasurface”, *Nat Commun* **13**, 7848 (2022) 10.1038/s41467-022-34197-6.
- [27] K. Wang, M. Chekhova, and Y. Kivshar, “Metasurfaces for quantum technologies”, *Phys. Today* **75**, 38–44 (2022) 10.1063/PT.3.5062.
- [28] Y. Kan and S. I. Bozhevolnyi, “Advances in Metaphotonics Empowered Single Photon Emission”, *Adv. Opt. Mater.* **11**, 2202759 (2023) 10.1002/adom.202202759.
- [29] J. Ma, J. Zhang, J. Horder, A. A. Sukhorukov, M. Toth, D. N. Neshev, and I. Aharonovich, “Engineering Quantum Light Sources with Flat Optics”, *Adv. Mater.*, 2313589 (2024) 10.1002/adma.202313589.
- [30] T. Santiago-Cruz, A. Fedotova, V. Sultanov, M. A. Weissflog, D. Arslan, M. Younesi, T. Pertsch, I. Staude, F. Setzpfandt, and M. Chekhova, “Photon pairs from resonant metasurfaces”, *Nano Lett.* **21**, 4423–4429 (2021) 10.1021/acs.nanolett.1c01125.
- [31] T. Santiago-Cruz, S. D. Gennaro, O. Mitrofanov, S. Addamane, J. Reno, I. Brener, and M. V. Chekhova, “Resonant metasurfaces for generating complex quantum states”, *Science* **377**, 991–995 (2022) 10.1126/science.abq8684.
- [32] J. Noh, T. Santiago-Cruz, C. F. Doiron, H. Jung, J. Yu, S. J. Addamane, M. V. Chekhova, and I. Brener, “Fano interference of photon pairs from a metasurface”, *Light Sci. Appl.* **14**, 371 (2025) 10.1038/s41377-025-01998-5.

- [33] J. H. Zhang, J. Y. Ma, M. Parry, M. Cai, R. Camacho-Morales, L. Xu, D. N. Neshev, and A. A. Sukhorukov, “Spatially entangled photon pairs from lithium niobate nonlocal metasurfaces”, *Sci. Adv.* **8**, eabq4240 (2022) 10.1126/sciadv.abq4240.
- [34] J. Y. Ma, J. H. Zhang, Y. X. Jiang, T. M. Fan, M. Parry, D. N. Neshev, and A. A. Sukhorukov, “Polarization engineering of entangled photons from a lithium niobate nonlinear metasurface”, *Nano Lett.* **23**, 8091–8098 (2023) 10.1021/acs.nanolett.3c02055.
- [35] W. H. Jia, G. Saerens, U. Talts, H. Weigand, R. J. Chapman, L. Li, R. Grange, and Y. M. Yang, “Polarization-entangled Bell state generation from an epsilon-near-zero metasurface”, *Sci. Adv.* **11**, eads3576 (2025) 10.1126/sciadv.ads3576.
- [36] J. Noh, T. Santiago-Cruz, V. Sultanov, C. F. Doiron, S. D. Gennaro, M. V. Chekhova, and I. Brener, “Quantum Pair Generation in Nonlinear Metasurfaces with Mixed and Pure Photon Polarizations”, *Nano Lett.* **24**, 15356–15362 (2024) 10.1021/acs.nanolett.4c04398.
- [37] J. Y. Ma, T. M. Fan, T. Haggren, L. V. Molina, M. Parry, S. Shinde, C. McManus-Barrett, J. H. Zhang, R. C. Morales, F. Setzpfandt, H. H. Tan, C. Jagadish, D. N. Neshev, and A. A. Sukhorukov, “Nonlinearity symmetry breaking for generating tunable quantum entanglement in semiconductor metasurfaces”, *Sci. Adv.* **11**, eadu4133 (2025) 10.1126/sciadv.adu4133.
- [38] J. Y. Ma, J. L. Ren, J. H. Zhang, J. J. Meng, C. McManus-Barrett, K. B. Crozier, and A. A. Sukhorukov, “Quantum imaging using spatially entangled photon pairs from a nonlinear metasurface”, *eLight* **5**, 2 (2025) 10.1186/s43593-024-00080-8.
- [39] M. A. Weissflog, J. Y. Ma, J. H. Zhang, T. M. Fan, S. Lung, T. Pertsch, D. N. Neshev, S. Saravi, F. Setzpfandt, and A. A. Sukhorukov, “Directionally tunable co- and counter-propagating photon pairs from a nonlinear metasurface”, *Nanophotonics* **13**, 3563–3573 (2024) 10.1515/nanoph-2024-0122.
- [40] D. A. Bykov, L. L. Doskolovich, A. A. Morozov, V. V. Podlipnov, E. A. Bezas, P. Verma, and V. A. Soifer, “First-order optical spatial differentiator based on a guided-mode resonant grating”, *Opt. Express* **26**, 10997–11006 (2018) 10.1364/OE.26.010997.
- [41] H. Wang, C. Guo, Z. Zhao, and S. Fan, “Compact incoherent image differentiation with nanophotonic structures”, *ACS Photonics* **7**, 338–343 (2020) 10.1021/acsphotonics.9b01465.
- [42] J. E. Harvey and R. N. Pfisterer, “Understanding diffraction grating behavior: including conical diffraction and Rayleigh anomalies from transmission gratings”, *Opt. Eng.* **58**, 087105 (2019) 10.1117/1.OE.58.8.087105.
- [43] B. DOUGHERTY, “On the average of a function and the mean value theorem for integrals”, *Pi Mu Epsilon J.* **14**, 251–254 (2016), <https://www.jstor.org/stable/48568127> (visited on 03/31/2025).
- [44] L. D. Hutcheson, “Measuring coupling efficiency in single-mode channel waveguides: a new technique”, *Appl. Opt.* **19**, 2247–2250 (1980) 10.1364/AO.19.002247.
- [45] A. V. Oppenheim and R. W. Schafer, *Discrete-time signal processing*, eng, Third edition., Prentice Hall signal processing series (Pearson, Upper Saddle River [N.J], 2010).